Supporting Information for

Monitoring Protein-Protein Interactions in the Cyanobacterial Circadian Clock in Real Time via Electron Paramagnetic Resonance Spectroscopy

Gary K. Chow,[†] Archana G. Chavan,[‡] Joel Heisler,[§] Yong-Gang Chang,[‡,^] Andy LiWang,[*,‡,§,∥,⊥,#,□] R. David Britt[*,†]

[†]Department of Chemistry, University of California, Davis, CA 95616

[‡]School of Natural Sciences, [§]Chemistry and Chemical Biology, [∥] Quantitative and Systems Biology, [⊥]Health Sciences Research Institute, and [#]Center for Cellular and Biomolecular Machines, University of California, Merced, CA 95343

[□]Center for Circadian Biology, University of California, San Diego, La Jolla, CA 92093.

Corresponding Authors

*Andy LiWang – Email: aliwang@ucmerced.edu. Phone: (209) 777-6341.

*R. David Britt – Email: rdbritt@ucdavis.edu. Phone: (530) 752-6377.

Present address

^Y.G.C.: Monash Biomedicine Discovery Institute, Monash University, Clayton VIC, 3800, Australia.

CONTENTS

PROTEIN QUALITY CONTROL

Figure S1. Intact LCMS of $N19C_{3IAP}$ demonstrates complete spin labelling

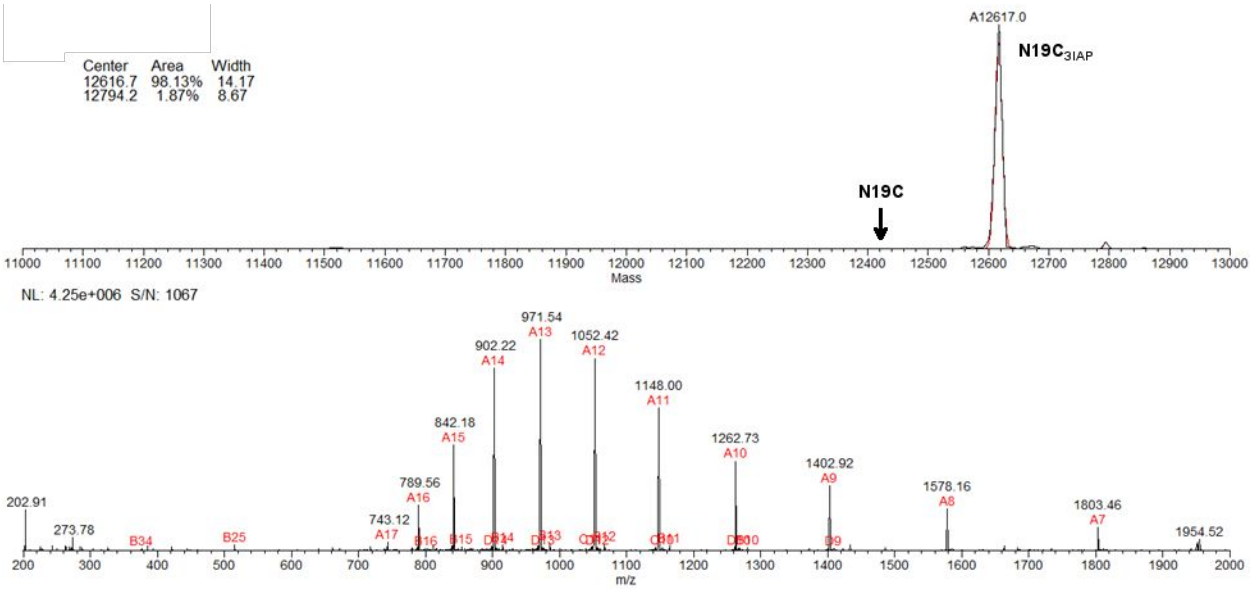

Top: transformed spectrum. Bottom: raw spectrum. LCMS masses: $N19C_{3IAP}$ (Calc: 12617.68; Found: 12617.0).

Figure S2. Native-PAGE of WT-KaiB and $N19C_{3IAP}$ binding to $KaiC_{EE}$.

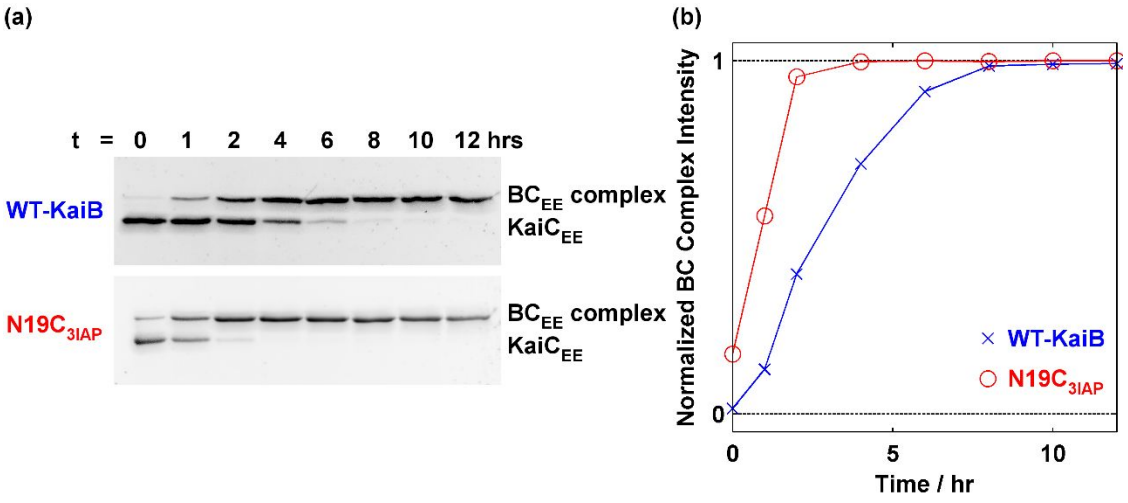

(a) Native-PAGE of samples collected at various time points from initial mixing of KaiB and $KaiC_{EE}$ as indicated on top of the images. Only KaiC-containing bands are shown. Species assignment is shown on the right. (b) KaiB-$KaiC_{EE}$ complexation estimated by densitometry. Traces refer to WT-KaiB (blue crosses) and $N19C_{3IAP}$ (red circles).

Figure S3. Fluorescence anisotropy assay on functionality of $N19C_{3IAP}$ in the in vitro oscillator reaction.

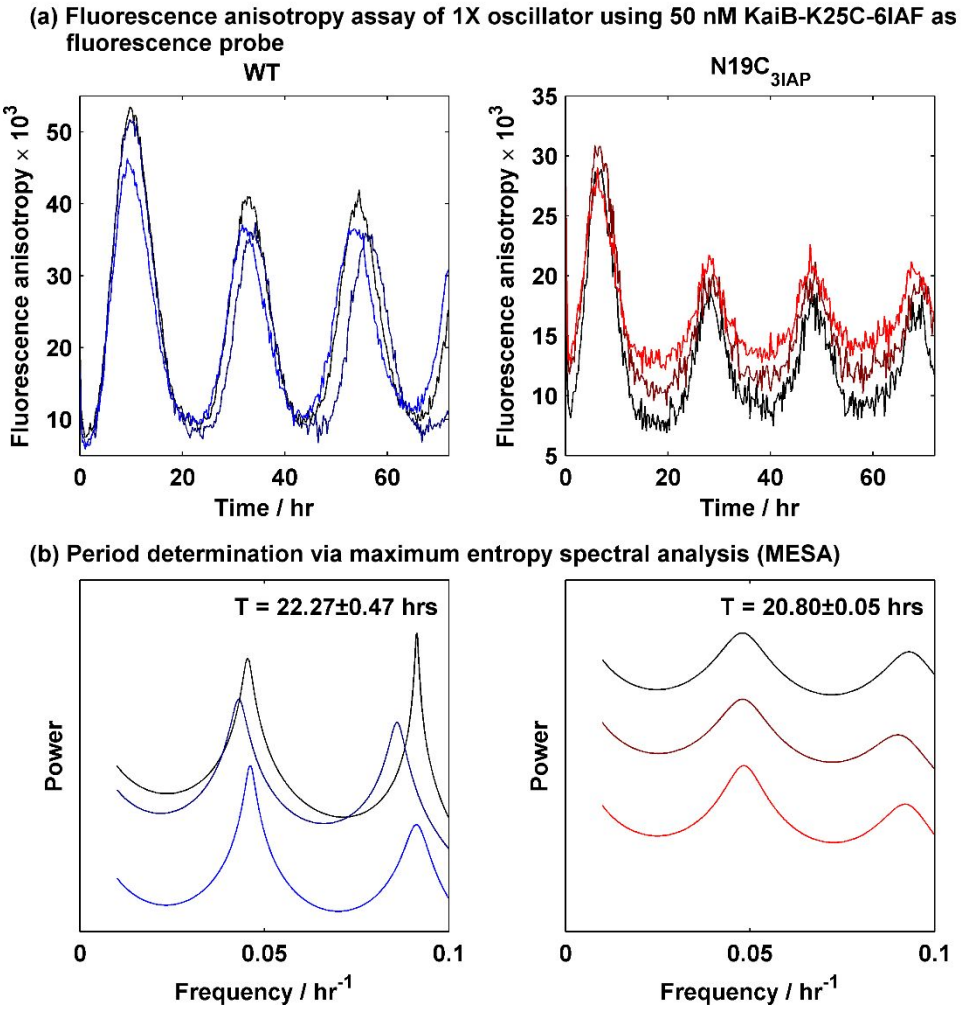

(a) Real-time fluorescence anisotropy traces of 1X oscillator reactions using WT-KaiB (blue) and $N19C_{3IAP}$ (red). In each plot, the three traces of varying brightness show results from technical triplicates. (b) Corresponding periodograms computed using maximum entropy spectral analysis (MESA) with the mean and SEM of the periods shown (n = 3).

EPR DATA PREPROCESSING

Figure S4. Microwave frequency drift correction.

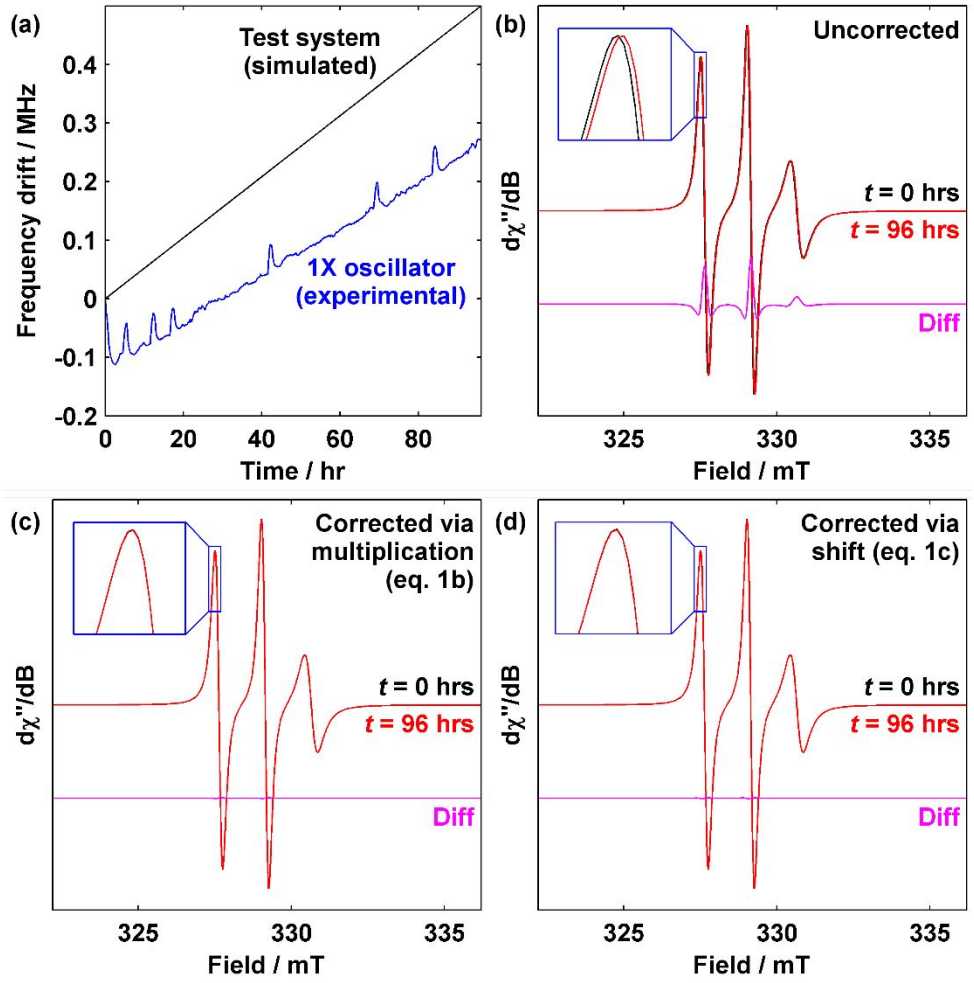

(a) Frequency drift plot of idealized test system (black) and experimental frequency drift observed in 1X $N19C_{3IAP}$ oscillator (blue). (b) Effect of microwave frequency drift on simulated spectrum at the beginning (black) and end (red) of the experiment. The difference spectrum is shown in magenta. See Table S1 for simulation details. (c) and (d) Demonstration of effectiveness of drift correction via multiplication (eq. 1b) or shift (eq. 1c) with identical coloring schemes as (b). Insets in (b)-(d) show zoomed in view of the boxed region.

Figure S5. Background correction.

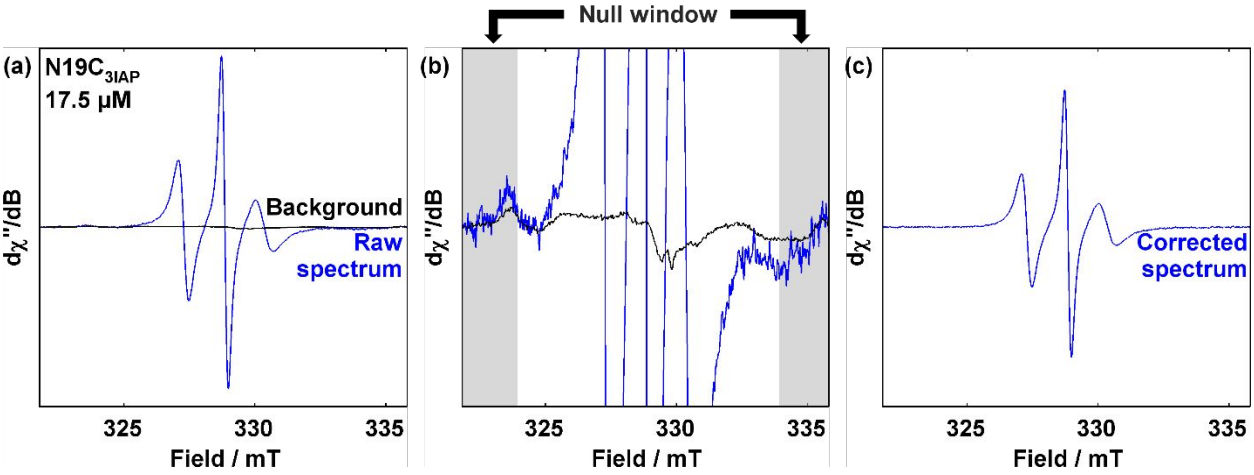

(a) Comparison of raw spectrum of $N19C_{3IAP}$ (blue) overlaid with background (black). (b) Expanded view of (a) to show the structure of the background signal showing trace manganese signals from the resonator cavity. Shaded area shows null window used in determining the magnitude of background necessary for background correction. (c) Background corrected spectrum.

Figure S6. Observation and evaluation of impact of time-dependent "*B*-shift".

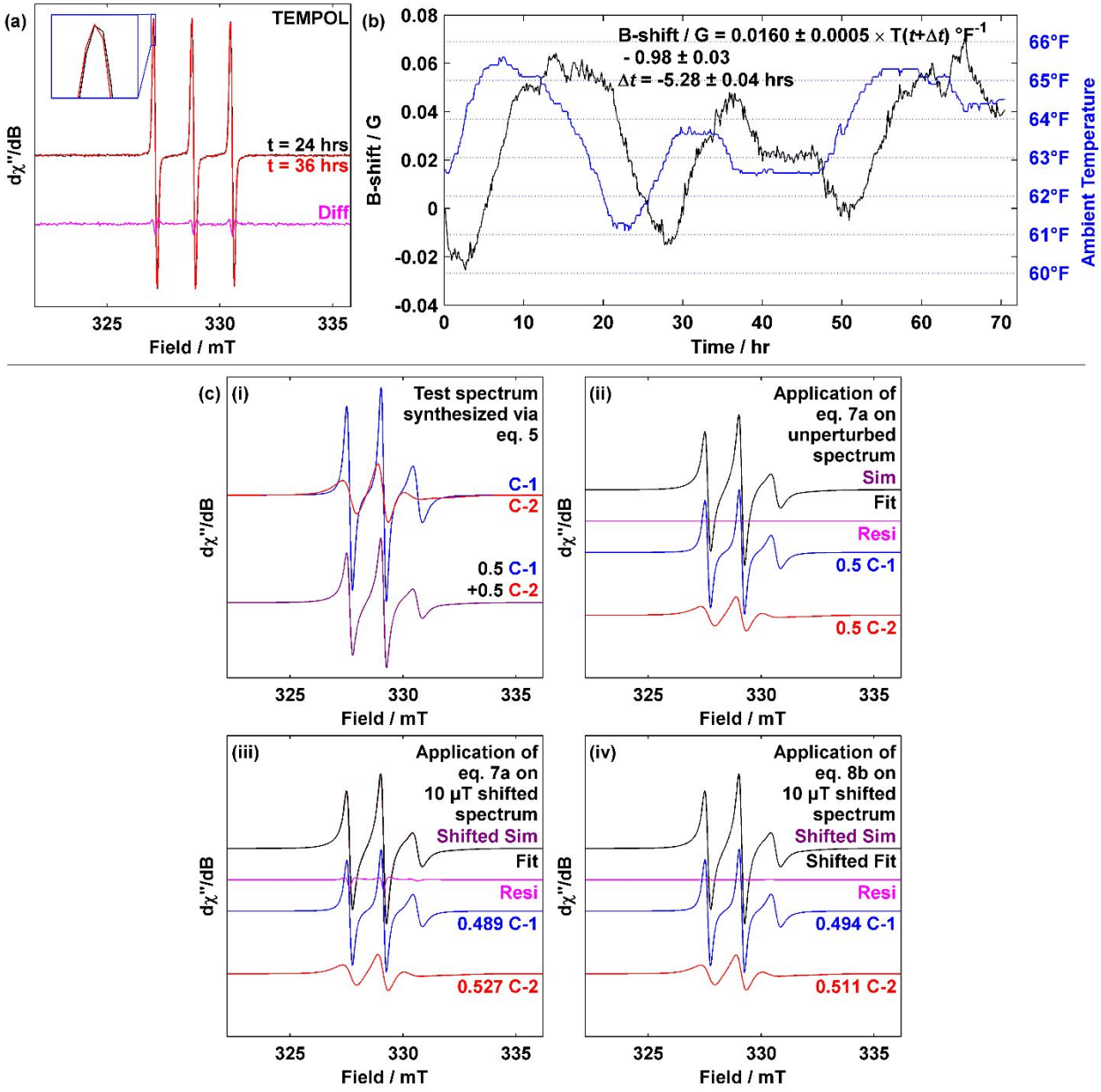

(a) cw-EPR spectrum of TEMPOL (20 μM) collected at 24 (black) and 36 (red) hrs after beginning acquisition. The difference is shown in magenta. (b) Plot of experimental "*B*-shift" (black) and variations in ambient temperature (blue) over 3 days. (c) Evaluation of the effect of "*B*-shift" on ratiometric spin quantification. (i) Motional components C-1 (τ_c = 1 ns, blue) and C-2 (τ_c = 3.16 ns, red) and synthesized spectrum using their weighted sum (purple). (ii) Solving for

weights of C-1 and C-2 via linear regression (eq. 7a) and the resultant spectrum (black) overlaid on synthesized spectrum in (i). (iii) Solving for weights of C-1 and C-2 via linear regression (eq. 7a) on the synthesized spectrum in (i) that has been shifted by 10 μT. (iv) Solving for weights of C-1 and C-2 via nonlinear regression with simultaneous fitting of "*B*-shift" (eq. 8b) on the synthesized spectrum in (i) that has been shifted by 10 μT. Residuals in (ii)-(iv) are shown in magenta.

QUALITATIVE EPR SPECTRAL FITTING

Table S1. Parameters used in illustrating the effect of motion on nitroxide cw-EPR spectra.

	Figure	g	A / MHz	$\log_{10}(\tau_c/\mathrm{ns})$	Phenomenological linewidth (Gaussian/Lorentzian) / MHz
Test System	2b	[2.0086, 2.0060, 2.0023]	[12, 16, 100]	-11	[0, 0.05]
				-10	
	2b, S4, S6			-9	
	2b, S6			-8.5	
				-8	
	2b			-7.5	
				-7	
				Rigid limit	[0.2, 0.2]

Microwave frequency was set to 9.24 GHz and simulated spectra were modulated at 0.19 mT to emulate experimental conditions.

Figure S7. Stacked plot of $N19C_{3IAP}$-$KaiC_{EE}$ reaction spectra.

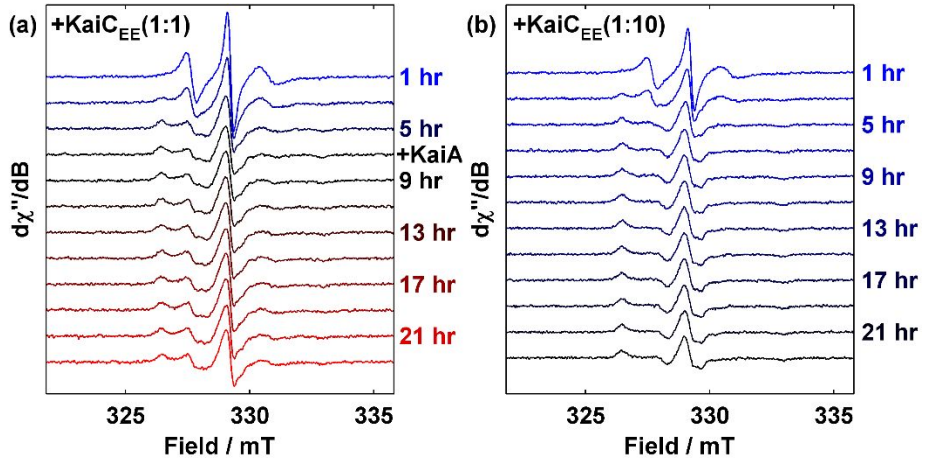

Reactions were performed with $N19C_{3IAP}$-$KaiC_{EE}$ ratios of (a) 1:1 and (b) 1:10 respectively using 17.5 μM $N19C_{3IAP}$. Spectra shown above are background corrected. In (a), KaiA was spiked at *t* = 7 hrs.

Figure S8. Fitting of $N19C_{3IAP}$-$KaiC_{EE}$ reaction spectra using slow-motion nitroxide spin model.

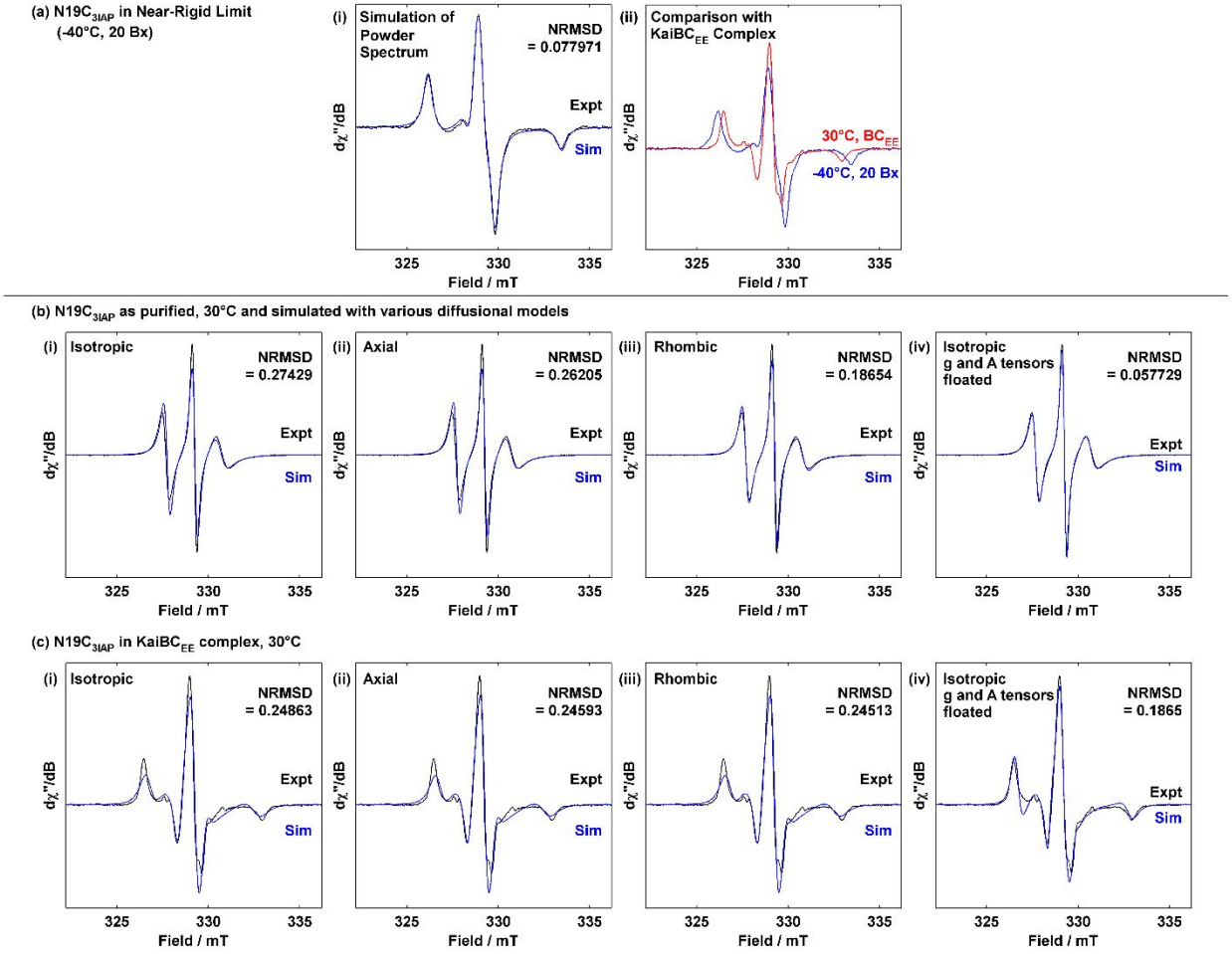

(a) cw-EPR spectrum of $N19C_{3IAP}$ at -40°C with 20% w/w sucrose (20 Bx) with (i) its simulations and (ii) in comparison with $KaiC_{EE}$-bound $N19C_{3IAP}$ shows that the latter is not in the solid-state regime. (b) and (c) Comparison of experimental and simulated spectra for free and KaiC-bound $N19C_{3IAP}$ respectively using (i) isotropic, (ii) axial and (iii) rhombic rotational diffusion models, and (iv) isotropic rotational diffusion while floating *g* and *A* tensors away from their rigid limit values. Refer to Table S2 for simulation parameters.

Table S2. Summary of spin parameters determined by least squares fitting of experimental $N19C_{3IAP}$ spectra.

g and *A* are listed in the order of *xx*, *yy* and *zz*. For τ_c, axial values are listed in the order of τ_{xy} and τ_z whereas rhombic values are listed in the order of τ_x, τ_y and τ_z. Square brackets indicate magnetic field bootstrap estimated 95% CI, $n_{bootstrap} = 200$.

N19C$_{3IAP}$		**Figure**	***g***	***A* / MHz**	**τ_c^{expt} / ns**	**Lw / mT***	**NRMSD**
Near-rigid Limit (20Bx, 233K)		S8a	2.0082, 2.0063, 2.00232; [2.0080, 2.0084], [2.0062, 2.0064], [2.00228, 2.00239]	17.1, 11.7, 102.28; [16.1, 18.6], [9.9, 13.3], [102.03, 102.48]	-	0.21, 0.28; [0.18, 0.30], [0.26, 0.30]	0.078
***g*, *A* fixed**	KaiB	S8bi			1.9; [1.8, 2.1]	-	0.274
		S8bii			1.8, $10^{5\#}$; [1.7, 2.0], [#]	-	0.262
		3f, S8biii			2.6, 1.1, $10^{5\#}$; [2.5, 2.7], [1.0, 1.2], [#]	-	0.187
	Kai(A)BC	S8ci			7.7; [7.3, 8.2]	-	0.249
		S8cii			7.8, 3.2; [7.2, 8.2], [2.0, 5.4]	-	0.246
		3f, S8ciii			7.0, 9.1, 3.6; [6.5, 7.3], [7.8, 10.3], [2.2, 6.3]	-	0.245
***g*, *A* floated**	KaiB	S8biv	2.0067, 2.0067, 2.0039	30, 15, 88	3.2	-	0.058
	Kai(A)BC	S8civ	2.0078, 2.0074, 2.0021	19, 13, 100	15.4	-	0.187

* Phenomenological Gaussian and Lorentzian peak-to-peak linewidths in mT.

Poorly constrained (reached lower or upper bound of parameter search space).

Table S3. Rotational correlation time estimated by Stokes-Einstein relation.

Structure (PDB)		**Monomeric fs-KaiB (5JWR)**	**Tetrameric gs-KaiB (4KSO)**	**KaiC-bound Kai-B (5JWQ)**
Approximate Shape and Dimension / nm		Sphere $r = 1.6$	Oblong	Cube $l = 10$
Molecular mass / g mol^{-1} (*)		11436	45745	413848
Approximate Volume / nm^3	Crystal structure	17.2	≈ 17.2 × 4 = 68.8	1000
	Specific volume	13.9	55.5	501.8
Stokes-Einstein Estimated τ_c (τ_c^{SE}) at 303 K / ns	Crystal structure	3.27	13.1	191
	Specific volume	2.64	10.6	95.7
Experimental N19C$_{3IAP}$ τ_c ($\tau_{c,iso}^{expt}$) / ns		-	1.9; [1.8, 2.1]	7.7; [7.3, 8.2]

* Wildtype sequences were used to calculate molecular mass.

Figure S9. Detection of KaiA-N19C$_{3IAP}$ interactions and spectral simulations.

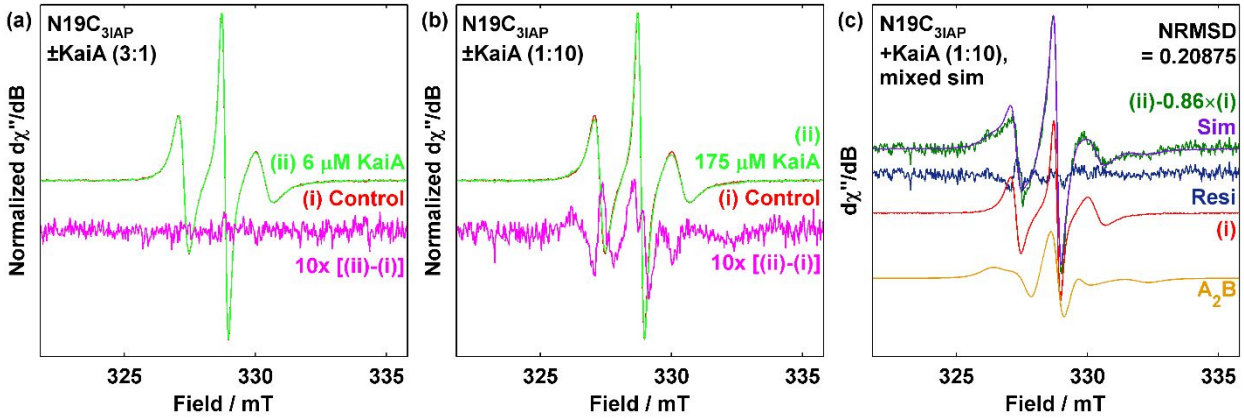

(a) and (b) comparison of cw-EPR spectra acquired with 17.5 μM N19C$_{3IAP}$ (red) against N19C$_{3IAP}$ equilibrated with 6 μM (a) and 175 μM (b) KaiA (light green). Spectra were normalized by their maximum intensity. The difference is shown in magenta below. (c) Semiphenomenological fitting (purple) of subtraction spectrum (green) obtained from (b) to a sum of free N19C$_{3IAP}$ (red) and KaiA$_2$B complex (orange). Residual is shown in dark blue. Refer to Table S4 for simulation parameters.

Table S4. Estimation of KaiB-KaiA direct binding dissociation constant.

Spectral changes were observed when $N19C_{3IAP}$ was equilibrated with tenfold excess KaiA. The new species was assumed to be A_2B and its quantity was estimated via spectral subtraction and simulation. The *g* and *A* values were fixed from Table S2 whereas isotropic τ_c and weight were floated. Square brackets indicate magnetic field bootstrap estimated 95% CI, $n_{bootstrap} = 200$.

$N19C_{3IAP}$ + 10x KaiA (A_2B)	**Figure**	**τ_c^{expt} / ns**	**Weight in subtraction spectrum / %**	**Weight in original spectrum / %**	**K_D^{app} / mM[#]**	**NRMSD**
	S9c	5.3 [4.6, 6.2]	56 [53, 59]	7.8 [7.4, 8.2]	1.0 [0.96, 1.1]	0.209

* Magnetic field bootstrapping produced a narrow distribution of best fit values likely because the parameter set entered a local minimum in the search space.

[#] Estimated by assuming the reaction

$$A_2 + B \rightleftharpoons A_2B; K_D^{app} = \frac{[A_2][B]}{[A_2B]}$$

without accounting for KaiB tetramer-monomer equilibrium, $[B]_0 = 17.5$ μM and $[A_2]_0 = 87.5$ μM. This calculation is only performed as a rough estimate of the KaiA-KaiB interaction strength. Note that the subtraction-simulation-quantification procedure places a lower limit on the fraction of A_2B and consequently an upper limit of K_D^{app}. See Supplementary Text for details.

QUANTITATIVE CW-EPR FITTING BASED KINETICS

Figure S10. Determination of scaling factor between B_{free} and B_{bound}.

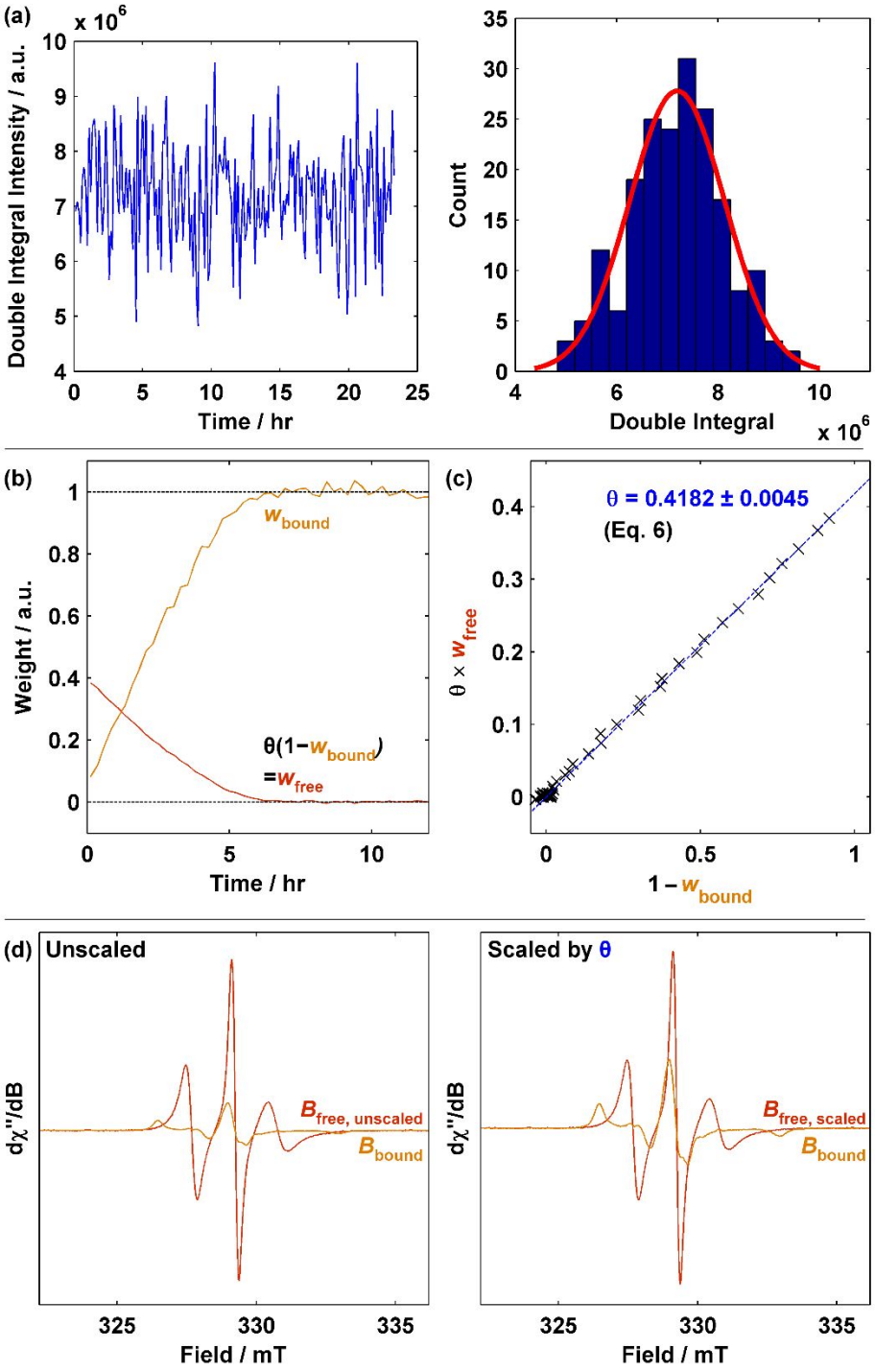

$N19C_{3IAP}$ was incubated with tenfold $KaiC_{EE}$ and cw-EPR spectra were collected over 24 hours. (a) Normalization of spectra via double integral is prone to noise and baseline induced errors. Left: time dependence of numerical double integral. Right: histogram and fit to Gaussian distribution of numerical double integral. (b) Fitting of weights without spectral scaling produces non-unity sums of weights. (c) Plot of weights of free KaiB against KaiC-bound KaiB weights. The error in θ shows 95% CI from linear regression. (d) Plot of unscaled (left) and scaled (right) spectra used for quantification of KaiC-bound KaiB. For (b) and (d), free KaiB is shown in red whereas KaiC-bound KaiB is shown in orange.

Figure S11. Quantitative $N19C_{3IAP}$-$KaiC_{EE}$ binding at 5X protein concentrations.

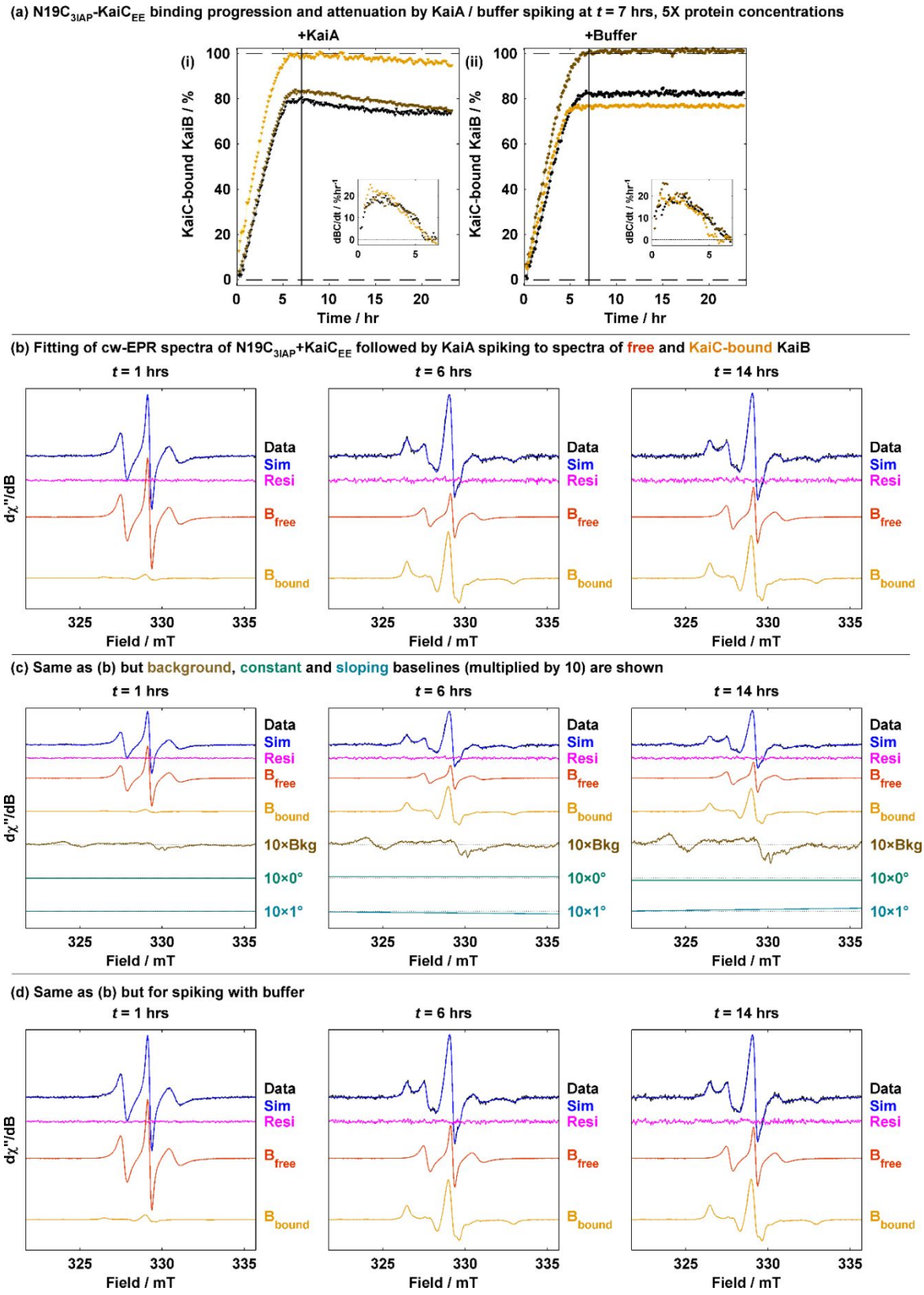

Kinetics and fitting of 5X $KaiC_{EE}$ phosphomimetic reaction with $N19C_{3IAP}$ at 1:1 stoichiometry followed by spiking with KaiA or buffer at $t \sim 7$ hrs. (a) Binding progression curve of triplicates of addition with KaiA (left) or buffer (right). Insets show binding velocity of corresponding experiments via Savitzky-Golay smoothing with 7-point window and 2nd order polynomials prior spiking. (b) Fitting of spectra for one replicate of KaiA spiking (brown trace in ai) using standard spectra of $N19C_{3IAP}$ and $N19C_{3IAP}$ in a tenfold excess of $KaiBC_{EE}$ at selected timepoints. Background and baseline components have been subtracted from both experimental and simulated data. (c) Same as (b) but background (brown) and baseline (constant / 0°, turquoise and linear / 1°, light blue) components are shown and multiplied by a factor of ten. (d) Same as (b) but buffer was spiked instead (black trace in aii).

Figure S12. Quantitative $N19C_{3IAP}$-$KaiC_{EE}$ binding at 1X protein concentrations.

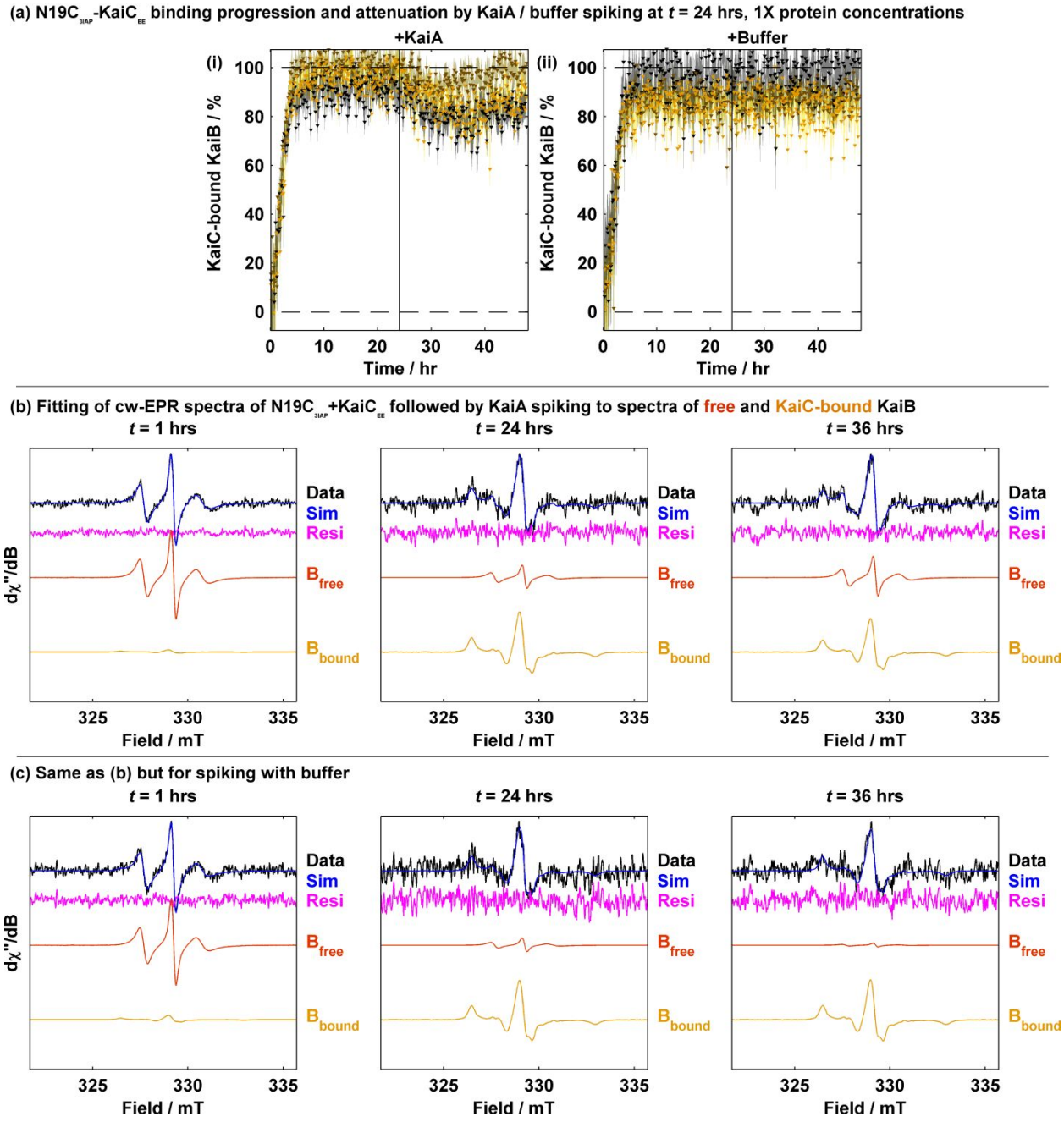

Kinetics and fitting of 1X $KaiC_{EE}$ phosphomimetic reaction with $N19C_{3IAP}$ at 1:1 stoichiometry followed by spiking with KaiA or buffer at $t \sim 24$ hrs. (a) Binding progression curve of triplicates of addition with KaiA (left) or buffer (right). (b) Fitting of spectra for one replicate of KaiA spiking (black trace in ai) using standard spectra of $N19C_{3IAP}$ and $N19C_{3IAP}$ in a tenfold excess of

$KaiBC_{EE}$ at selected timepoints. Background and baseline components have been subtracted from both experimental and simulated data. (c) Same as (b) but buffer was spiked instead (black trace in aii).

Figure S13. Raw data of fluorescence anisotropy based KaiB-KaiC$_{EE}$ binding assay.

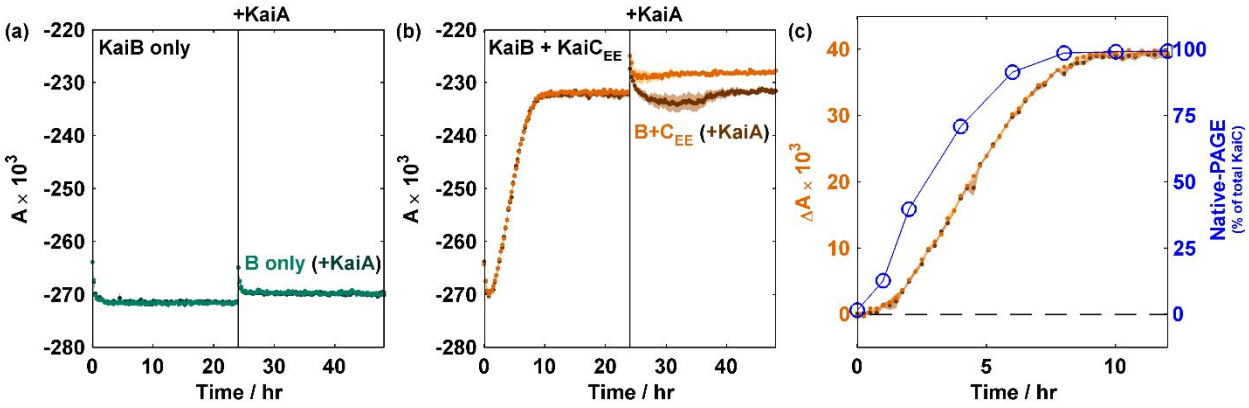

Fluorescence anisotropy of KaiB-K25C-6IAF (K25C$_{6IAF}$, 50 nM) in 3.45 μM WT-KaiB in the absence (a, turquoise) and presence (b, orange) of KaiC$_{EE}$, 3.5 μM. Shaded areas show SEM (n = 3). Black line at t = 24 hrs indicate time at which 1.2 μM KaiA (dark turquoise in (a), brown in (b)) or buffer (turquoise in (a), orange in (b)) was spiked. (c) Comparison of native-PAGE (blue hollow circles) and baseline subtracted fluorescence anisotropy (brown) in the time window t = 0 – 12 hrs.

Figure S14. Real-time cw-EPR data analysis of $N19C_{3IAP}$-KaiC binding in the 1X oscillator.

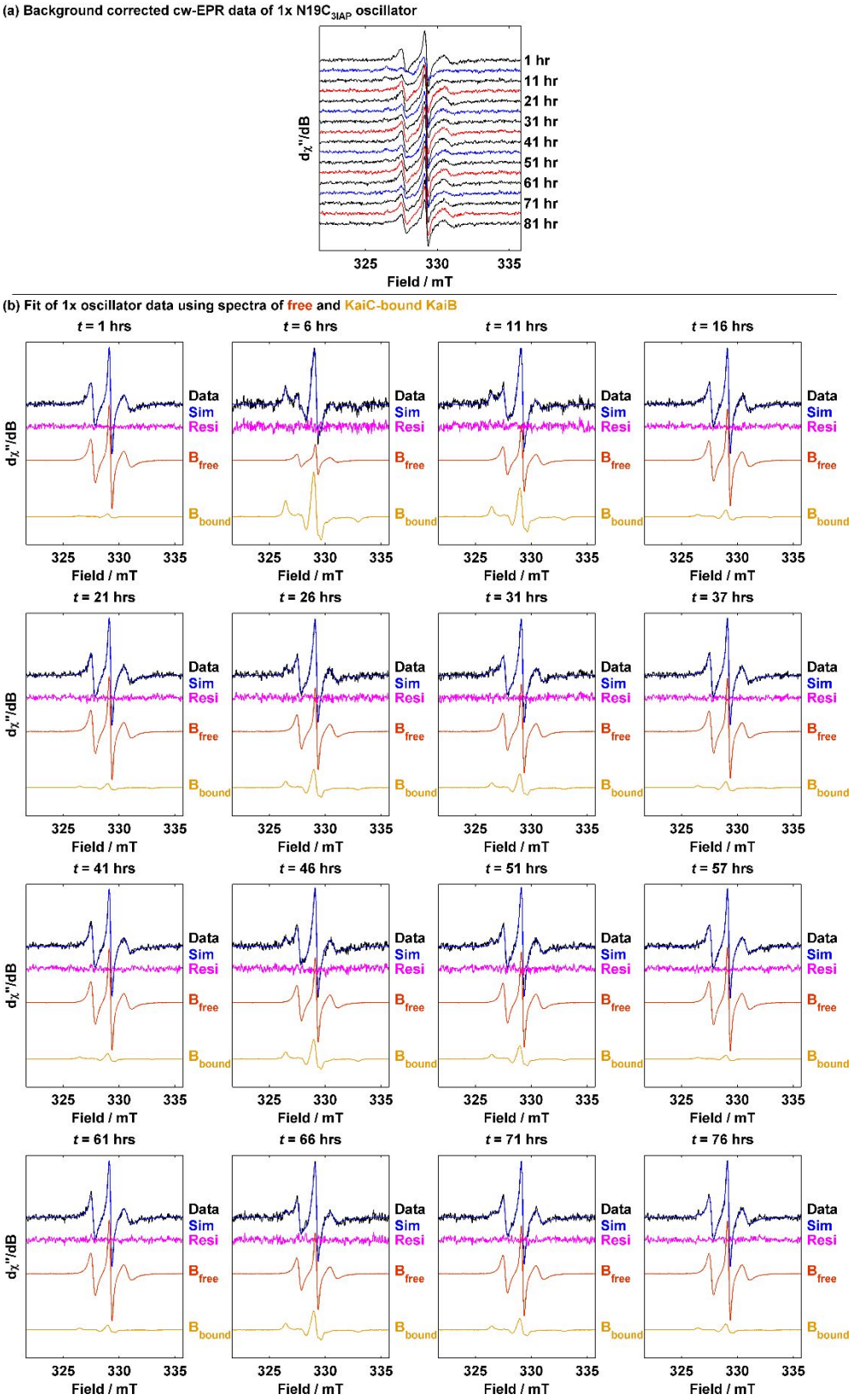

(a) Stacked plot of ~1-hour binned spectra (8 unbinned spectra). (b) Simulation of spectra at 5-hour intervals. Note that the times are not at regular 5-hour intervals due to slight deviation of spectral acquisition time from 7.5 minutes per spectrum.

Figure S15. Reproducibility of the 1X N19C$_{3IAP}$ oscillator.

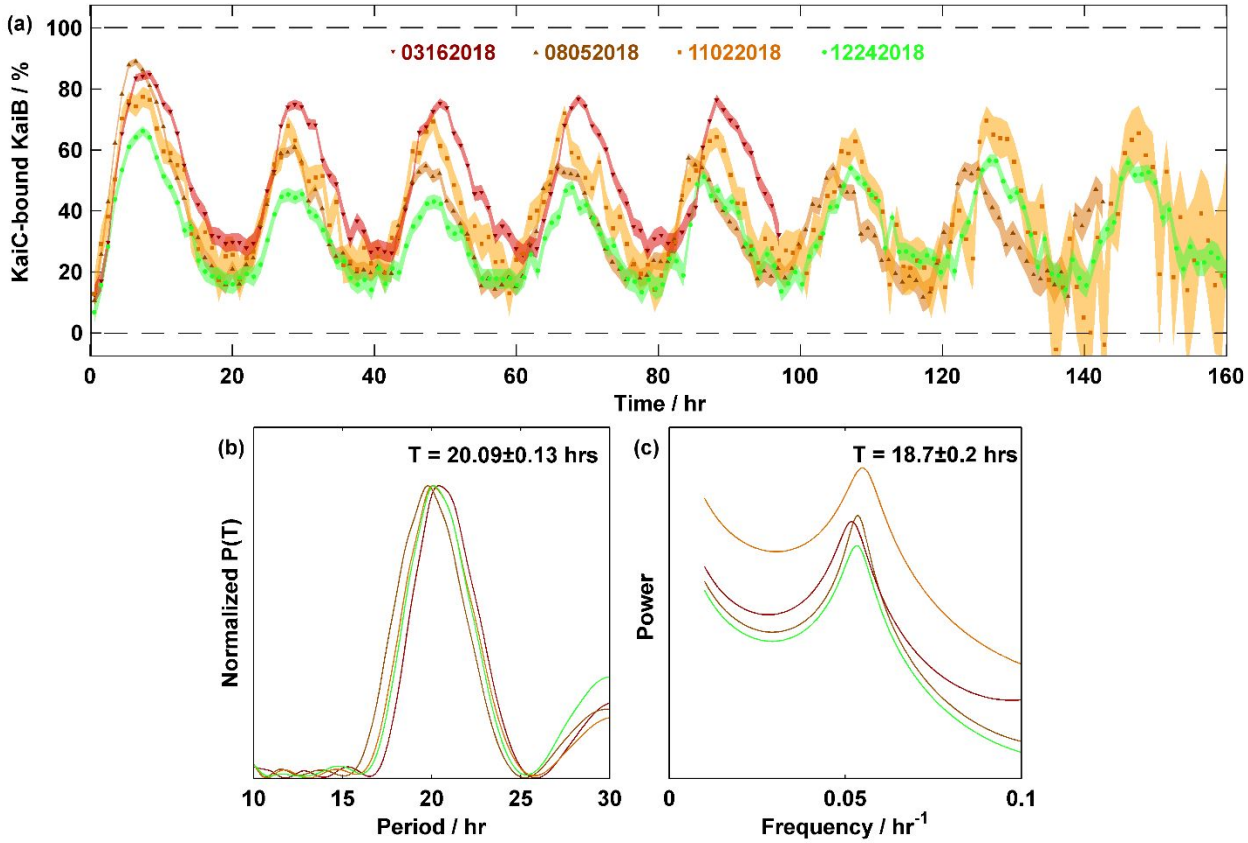

The 1X N19C$_{3IAP}$ oscillator was repeated 4 times in 4 different weeks. (a) cw-EPR derived kinetics of all trials. Trial 1 (dark red downward facing triangles), Trial 2 (brown upward facing triangles), Trial 3 (orange squares) and Trial 4 (light green circles). Data were binned by 1-hour bins. Shaded area shows 95% CI. (b) Lomb-Scargle periodogram. (c) Maximum entropy spectral analysis. For (b) and (c), the color schemes follow (a) whereas the periods are given in mean ± SEM format.

Figure S16. Phenomenological fitting of $N19C_{3IAP}$-KaiC binding with sum of cosines.

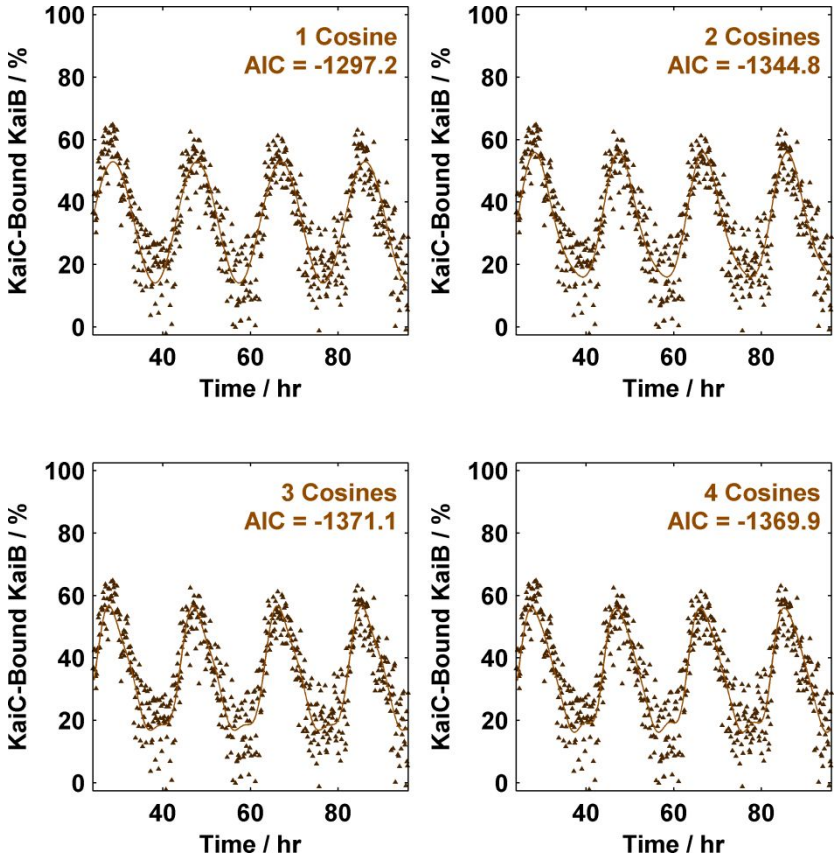

Upward facing triangles indicate cw-EPR based kinetics. Dash-dot line indicates fit to sum of cosines. The data shown is the same trial as Fig. 5, and Trial 2 in S15 and Table S5.

Table S5. mFourfit parameters of $N19C_{3IAP}$ 1X oscillator data.

$N19C_{3IAP}$ 1x oscillator mFourfit parameters for oscillation of fraction of KaiC-bound KaiB over time determined by nonlinear least squares for four independent trials. Parameters shown were determined from unbinned data between t = 24 – 97 hrs (~0.125 hour per point). Errors shown are 95% confidence interval (CI) via the Jacobian matrix.

Trial 1 (03162018, dark red downward facing triangles in Fig. S15)

q	1	2	3	4
C / %	48.3 ± 0.6	48.3 ± 0.6	48.3 ± 0.6	48.3 ± 0.6
T / hr	20.03 ± 0.11	20.04 ± 0.09	20.04 ± 0.08	20.04 ± 0.08
A_1 **/ %**	-23.7 ± 0.9	-23.6 ± 0.8	-23.5 ± 0.8	-23.5 ± 0.8
φ_1 **/ hr**	-0.38 ± 0.35	-0.35 ± 0.28	-0.36 ± 0.27	-0.36 ± 0.27
A_2 **/ %**	-	5.2 ± 0.8	5.3 ± 0.8	5.3 ± 0.8
φ_2 **/ hr**	-	-1.72 ± 0.34	-1.70 ± 0.33	-1.69 ± 0.33
A_3 **/ %**	-	-	1.7 ± 0.8	1.7 ± 0.8
φ_3 **/ hr**	-	-	0.50 ± 0.53	0.52 ± 0.53
A_4 **/ %**	-	-	-	-0.4 ± 0.8
φ_4 **/ hr**	-	-	-	-0.60 ± 1.64
$A_{peak\text{-}to\text{-}peak}$ **/ %**	47.4	50	48.7	48.1
RSS	3.63	2.83	2.74	2.74
p**(AIC)**	5	7	9	11
AIC	-1355.1	-1500.5	-1515.7	-1512.6

Trial 2 (08052018, brown upward facing triangles in Fig. S15, also in Fig. 5 and S14, S16)

q	1	2	3	4
C / %	33.5 ± 0.7	33.4 ± 0.6	33.3 ± 0.6	33.3 ± 0.6
T / hr	19.20 ± 0.14	19.21 ± 0.12	19.23 ± 0.11	19.22 ± 0.11
A_1 **/ %**	-19.4 ± 0.9	-19.5 ± 0.9	-19.5 ± 0.9	-19.5 ± 0.9
φ_1 **/ hr**	-0.21 ± 0.46	-0.21 ± 0.41	-0.25 ± 0.37	-0.24 ± 0.37
A_2 **/ %**	-	3.3 ± 0.9	3.4 ± 0.9	3.5 ± 0.9
φ_2 **/ hr**	-	-1.09 ± 0.54	-1.11 ± 0.49	-1.09 ± 0.49
A_3 **/ %**	-	-	2.5 ± 0.9	2.5 ± 0.9
φ_3 **/ hr**	-	-	0.99 ± 0.48	1.00 ± 0.48
A_4 **/ %**	-	-	-	-0.7 ± 0.9
φ_4 **/ hr**	-	-	-	-0.86 ± 0.97
$A_{peak\text{-}to\text{-}peak}$ **/ %**	38.8	39.9	39.8	39.8
RSS	4	3.67	3.49	3.47
p**(AIC)**	5	7	9	11
AIC	-1297.2	-1344.8	-1371.1	-1369.9

Trial 3 (11022018, orange squares in Fig. S15)

q	1	2	3	4
C / %	36.3 ± 1.3	36.1 ± 1.3	36.1 ± 1.3	36.1 ± 1.3
T / hr	19.67 ± 0.25	19.62 ± 0.23	19.61 ± 0.22	19.62 ± 0.22
A_1 **/ %**	-22.2 ± 1.9	-22.4 ± 1.8	-22.3 ± 1.8	-22.4 ± 1.8
φ_1 **/ hr**	-0.76 ± 0.81	-0.56 ± 0.74	-0.53 ± 0.73	-0.56 ± 0.72
A_2 **/ %**	-	4.2 ± 1.8	4.2 ± 1.8	4.2 ± 1.8
φ_2 **/ hr**	-	-12.07 ± 1.03	-12.02 ± 1.01	-12.07 ± 1.01
A_3 **/ %**	-	-	1.0 ± 1.8	0.9 ± 1.8
φ_3 **/ hr**	-	-	0.96 ± 1.93	1.00 ± 2.09
A_4 **/ %**	-	-	-	-1.2 ± 1.8
φ_4 **/ hr**	-	-	-	0.81 ± 1.31
$A_{\text{peak-to-peak}}$ **/ %**	44.4	47.1	46.7	49.2
RSS	15.9	15.4	15.4	15.3
p**(AIC)**	5	7	9	11
AIC	-465.61	-481.7	-478.91	-476.73

Trial 4 (12242018, light green circles in Fig. S15)

q	1	2	3	4
C / %	28.8 ± 0.7	28.7 ± 0.6	28.7 ± 0.6	28.7 ± 0.6
T / hr	19.70 ± 0.18	19.68 ± 0.16	19.68 ± 0.16	19.69 ± 0.15
A_1 **/ %**	-15.1 ± 0.9	-15.1 ± 0.9	-15.0 ± 0.9	-15.0 ± 0.9
φ_1 **/ hr**	-0.64 ± 0.60	-0.54 ± 0.54	-0.55 ± 0.52	-0.57 ± 0.50
A_2 **/ %**	-	2.6 ± 0.9	2.6 ± 0.9	2.6 ± 0.9
φ_2 **/ hr**	-	-1.26 ± 0.71	-1.22 ± 0.69	-1.24 ± 0.69
A_3 **/ %**	-	-	1.0 ± 0.9	1.0 ± 0.9
φ_3 **/ hr**	-	-	1.06 ± 1.01	1.11 ± 0.98
A_4 **/ %**	-	-	-	-1.1 ± 0.9
φ_4 **/ hr**	-	-	-	-0.11 ± 0.78
$A_{\text{peak-to-peak}}$ **/ %**	30.1	30.6	30.5	31.6
RSS	3.96	3.77	3.74	3.7
p**(AIC)**	5	7	9	11
AIC	-1302.4	-1329	-1330	-1331.7

SUPPLEMENTARY TEXT

Maximum error of frequency correction

In the methods section, two methods of frequency correction via multiplication of frequency ratio (eq. 1b) or addition by frequency difference (eq. 1c) were discussed and implemented. In both cases, because the magnetic field sweep window B_w is fixed by the settings used at t = 0 hrs with 1024 field points spanning 200 G, direct comparison between a spectrum collected at e.g. 9.2400 GHz $y_0(B_w)$ and 9.2405 GHz with the latter with corrected field positions $y_1(B_{w'})$ is not possible because their x-abscissa are different. This is solved by interpolating the frequency corrected spectrum to the original magnetic field positions via MATLAB routine `interp1` to convert $y_1(B_{w'})$ to $y_1(B_w)$. The interpolation procedure produces NaNs on the edges of the spectra which are then converted to zeroes for further processing. We note here that replacing these values with zeroes do not interfere with data analysis as the nitroxide transitions span only about 100 G even in the near-rigid limit at X-band (Fig. S8a).

The merits and maximum error introduced by the frequency correction methods shall be revisited below by rewriting the correction equations.

(1) Frequency correction via frequency ratio

Microwave frequency drift correction can be implemented by multiplying the frequency ratios of two spectra collected at slightly different frequencies.

$$B_1 = \frac{h\nu_1 - AI}{g\mu_B} + \ldots = \left(\frac{h\nu_0 - AI}{g\mu_B}\right)\left(\frac{\nu_1}{\nu_0}\right) + \frac{AI}{g\mu_B}\left(\frac{\nu_1}{\nu_0} - 1\right) + \ldots \approx \frac{B_0\nu_1}{\nu_0} \ldots (S1a)$$

The error term ε_{1b} is hence

$$\varepsilon_{1b} = \frac{AI}{g\mu_B}\left(\frac{\nu_1}{\nu_0} - 1\right)$$

Worst case scenario is achieved when the largest component of A, A_z, is considered in the near-rigid limit with minimized g.

$$\varepsilon_{1b,max} = \frac{(100\ \text{MHz})(6.626 \times 10^{-34}\text{J}\cdot\text{s})(1)}{(2.0023)(9.274 \times 10^{-24}\text{J}\cdot\text{T}^{-1})}\left(\frac{9.2405\ \text{GHz}}{9.2400\ \text{GHz}} - 1\right) \approx 2 \times 10^{-7}\text{T} = 2 \times 10^{-4}\text{mT}$$

Hence, equation 1b produces a maximum error of 2×10^{-4} mT, 2 orders of magnitude smaller than the magnetic field intervals (2×10^{-2} mT).

(2) Frequency correction via linear shift

Microwave frequency drift correction can be implemented by shifting the magnetic field axis linearly.

$$B_1 = \frac{h\nu_1 - AI}{g\mu_B} + \ldots = \frac{h\nu_1 - h\nu_0 + h\nu_0 - AI}{g\mu_B} + \ldots = B_0 + \frac{h(\nu_1 - \nu_0)}{g\mu_B} \ldots (\text{S1}b)$$

The error in the field correction ε_{1c} stems from anisotropy of g.

$$\varepsilon_{1c} = \frac{h(\nu_1 - \nu_0)}{\mu_B}\left(\frac{1}{g} - \frac{1}{g_e}\right)$$

Worst case scenario is achieved with the most anisotropic g-value.

$$\varepsilon_{1c,max} = \frac{(6.626 \times 10^{-34}\text{J}\cdot\text{s})(0.5\ \text{MHz})}{9.274 \times 10^{-24}\text{J}\cdot\text{T}^{-1}}\left|\frac{1}{2.0082} - \frac{1}{2.0023}\right| \approx 5 \times 10^{-8}\text{T} = 5 \times 10^{-5}\text{mT}$$

Hence, equation 1c produces a maximum error of 5×10^{-5} mT, which is almost 3 orders of magnitude smaller than the magnetic field intervals.

Thus, both methods produce magnetic field correction errors that are significantly less than the magnetic field intervals of the spectra collected and can be considered negligible. We note that (1c) gives a smaller maximum error than (1b) for the nitroxide system at X-band whereas we opted to use (1b) throughout the manuscript. The above calculations justify the use of either methods.

Estimation of KaiB-KaiA direct binding dissociation constant.

In the main text, Fig. S9 and Table S4, we attempted to estimate the dissociation constant between KaiA and KaiB based on N19C$_{3IAP}$-KaiA data alone. We mentioned that subtraction-simulation based quantification produced a lower limit on the fraction of KaiA-bound KaiB. To prove this assertion, consider the reaction again:

$$A_2 + B \rightleftharpoons A_2B$$

We assume that free KaiB and A_2B each possesses their respective spectra B_{free} and B_{A_2B} such that the real-time cw-EPR data matrix Y can be written as

$$Y = Bw = \begin{pmatrix} B_{\text{free}} & B_{A_2B} \end{pmatrix} \begin{pmatrix} w_{\text{free}} \\ w_{A_2B} \end{pmatrix} \ldots (\text{S2})$$

where w refers to the weights of the components. It is theoretically possible that the spin label redistributes its rotamer populations on binding KaiA such that B_{A_2B} partially resembles B_{free}:

$$B_{A_2B} = (1 - \phi)B_{\text{free}} + \phi B_c \ldots (\text{S3}a)$$

where $0 \leq \phi \leq 1$ is a tunable parameter describing the distinctness of B_{A_2B} from B_{free} whereas B_c is some unknown spectrum. We can rewrite eq. S2 as

$$Y = \begin{pmatrix} B_{\text{free}} & (1 - \phi)B_{\text{free}} + \phi B_c \end{pmatrix} \begin{pmatrix} w_{\text{free}} \\ w_{A_2B} \end{pmatrix} \ldots (\text{S3}b)$$

Using a change-of-basis matrix R, we get

$$Y = BRR^{-1}w, R = \begin{pmatrix} 1 & -\dfrac{1-\phi}{\phi} \\ 0 & \dfrac{1}{\phi} \end{pmatrix}, R^{-1} = \begin{pmatrix} 1 & 1-\phi \\ 0 & \phi \end{pmatrix} \ldots (\text{S4}a)$$

$$Y = (B_{\text{free}} \quad B_c)\begin{pmatrix} w_{\text{free}} + (1-\phi)w_{A_2B} \\ \phi w_{A_2B} \end{pmatrix} \ldots (\text{S4}b)$$

At ϕ = 0, B_{free} and B_{A_2B} are indistinguishable. As ϕ increases, the two states become spectroscopically distinct but some of the population in A_2B is misattributed to the population of free KaiB. When ϕ approaches 1, the spectra of the two states are distinct and A_2B is no longer misattributed to free KaiB. This analysis implies that quantification is accurate only if we can find conditions such that ϕ = 1. Spectral subtraction analysis thus relies on the assumptions that

(1) B_c is well modelled by a typical nitroxide experiencing some motional dynamics and

(2) ϕ = 1.

The assumptions are bypassed when binding saturation conditions can be found as in the case of $N19C_{3IAP}$-$KaiC_{EE}$. However, this was not achieved with the KaiA-KaiB system. We observed from Fig. S9c that assumption (1) was fulfilled in that the difference spectrum between tenfold excess KaiA versus control could be well simulated with a nitroxide undergoing isotropic Brownian rotational motion. As there is insufficient data to test assumption (2) without further manipulating KaiB, we qualitatively examine the impact of $\phi < 1$. Specifically, eq. S4b implies that $\phi < 1$ leads to overestimation of w_{free} and underestimation of w_{A_2B} and hence $[A_2B]$. The downstream effect of the latter is that the apparent dissociation constant

$$K_D^{app} = \frac{[A_2][B]}{[A_2B]} = \frac{([A_2]_0 - [A_2B])([B]_0 - [A_2B])}{[A_2B]}$$

is an overestimate.